Vrije Universiteit Brussel
Course: CERN Summer School

Dynamic thermal simulation of irradiated silicon sensors

Author:
Mathias Mancini

Academic year:
2017-2018

Supervisor:
Victor Coco
Course Titulars:
Freya Blekman
Steven Lowette

September 11, 2018

Abstract

A simulation is built to test the thermal behaviour of non uniformly irradiated silicon sensors for the VeloPix upgrade for the LHCb detector. The program contains tools to simulate the dynamic evolution of temperature sensitive quantities in the sensor and analyse them. The main features of the software include a simulation of heat sinks and sources, thermal radiation and internal heat generation coming from leakage currents, as well as the effects of radiation damage on this leakage current. The produced software has been tested with various case studies. The software is well documented and made public, it will be refined and validated in order to create a realistic simulation which will be compared with experiments.

Contents

1 The LHCb detector **3**
1.1 Detector Layout . . . 3
1.2 Vertex locator and its upgrade . . . 4
1.3 The silicon sensor . . . 5
1.3.1 Working principle . . . 5
1.3.2 Effects of irradiation . . . 7

2 Motivation **8**

3 Simulation **10**
3.1 Physics . . . 11
3.2 Analysis . . . 12

4 Validation **13**
4.1 Case study: Internal propagation . . . 13
4.2 Case study: Cooling mechanism (simple) . . . 15
4.3 Other case studies and finalising the validation . . . 15

5 Conclusion **17**

References **18**

1 The LHCb detector

The Large Hadron Collider beauty experiment has been designed to study heavy flavour physics at the LHC. The main purpose of this detector is to look for rare decays in B and D hadrons, as well as searching for new physics via high-precision CP violation measurements. In addition its forward coverage allows to complement the coverage of the ATLAS and CMS detectors in terms of SM production measurements.

1.1 Detector Layout

The LHCb detector is a one-sided spectrometer with an angular coverage from 10 mrad to 300 (250) mrad in the bending (non-bending) plane. Most of the high energy $b\bar{b}$ pairs are produced in a forward or backward cone with a very small angle with respect to the beam axis, motivating this geometry. The layout of the detector is shown in figure 1.

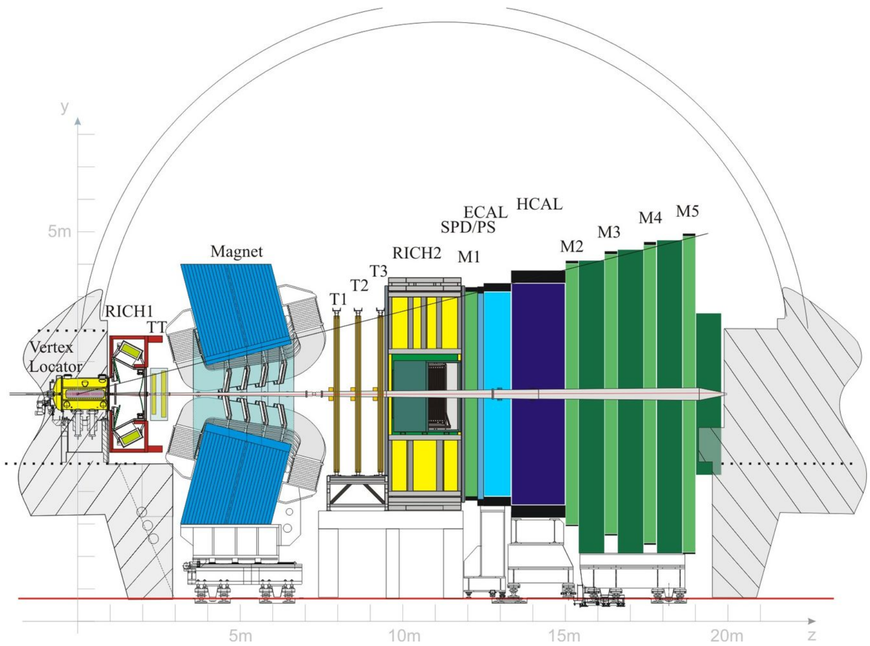

Figure 1: Cross section of the LHCb detector. Components: Vertex Locator (VELO), two RICH counters, four tracking stations (TT and T1-T3), Scintillating Pad Detector (SPD), Preshower (PS), Electromagnetic and Hadronic Calorimeters (ECAL, HCAL) and five muon stations (M1-M5). [1],[2],[3]

The main characteristics of the LHCb are:

- Excellent vertex and momentum resolution
- A robust and flexible trigger system

- Good particle identification capabilities

The vertex position and particle momentum resolution are necessary to obtain precise invariant mass and proper-time measurements, which are required to study the very rapidly oscillating B_s-$\bar{B}_s$ meson system [2]. The trigger system is set up to reduce the data intake from ∼40 MHz to 1 MHz via hardware (L0), then down to 5 kHz using software systems (HLT). The trigger keeps events featuring the key characteristics of the B meson decay, namely long lived particles, with well defined primary and secondary vertices with a large mass. A strong particle identification is essential to study the many possible hadronic decays of the mesons [1].

1.2 Vertex locator and its upgrade

The VErtex LOcator (VELO) is a fundamental part of the tracking system, with its closest measurement channel at 8 mm of the interaction region. It is complemented by the Tracker Turicencis upstream of the dipole magnet, downstream three tracking stations T1-T3 complete the rest of the tracker.

The current VELO subdetector consists of 21 station, each containing two modules with R- and ϕ- strip sensors. The layout is shown in figure 2 and the individual module setup in figure 3a. In 2019 during the second long shutdown of the LHC the VELO will be upgraded using hybrid pixel sensors, named VeloPix. It will be able to work without a trigger system and readout information at 40 MHz. A VeloPix station contains 24 ASICs (Application Specific Integrated Circuits) placed as shown in figure 3b. A VeloPix module, containing twelve ASICs, is cooled down to $-30°$ C using a microchannel substrate. The setup is shown in figure 4.

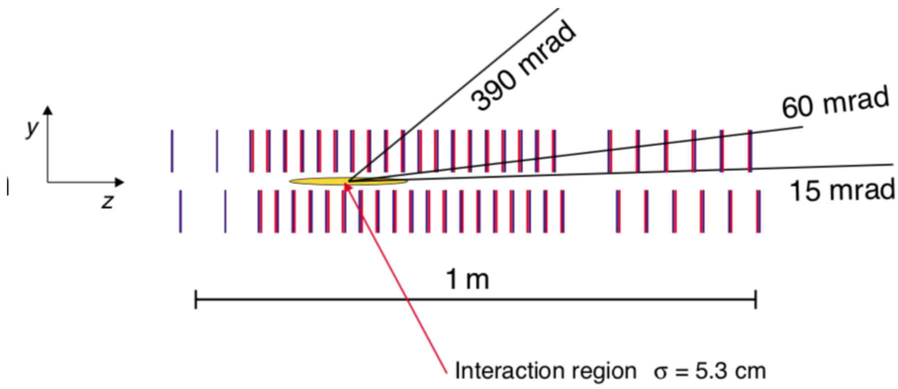

Figure 2: Arrangement of the stations along the beam axis, with a view of the cross section at x = 0. The blue lines indicate R-sensors and red lines ϕ-sensors. The three lines show the minimal and maximal angles covered as well as the average angle in minimum bias events. [4]

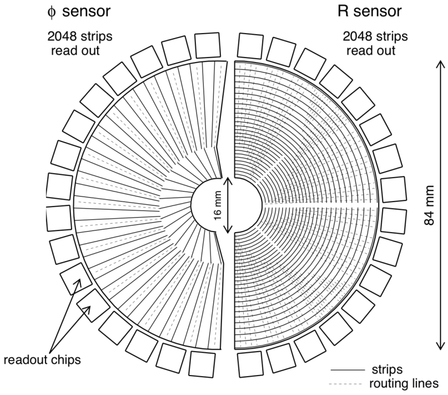

(a) Schematic of the VELO strip sensors. The R-sensors have strips with constant radius. The ϕ-sensors are split into two regions to equalise occupancy, and have strips along constant azimuthal angles. [4]

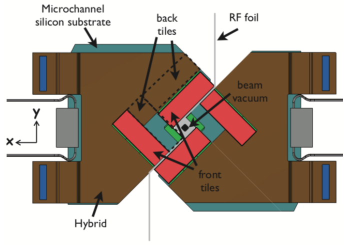

(b) Schematic of a VeloPix station. [5]

Figure 3

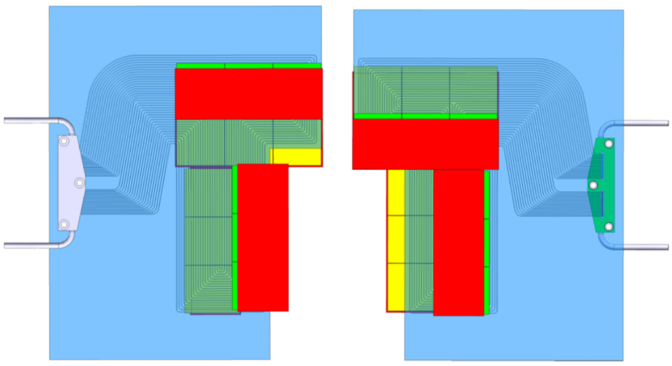

Figure 4: Front and rear side of a VeloPix module. Sensors are drawn in red and the microchannel cooling substrate in blue. [6]

1.3 The silicon sensor

In this section the working principle of a diode will be discussed in section 1.3.1. Using a silicon sensor in a harsh radiative environment will change its properties over time. The important consequences of the irradiation will be discussed in section 1.3.2.

1.3.1 Working principle

A PN diode consists in joining two pieces of semiconductor together, one with extra electrons and one with fewer electrons. The process of modifying the amount of electrons inside the material is called doping. This is achieved by contaminating the

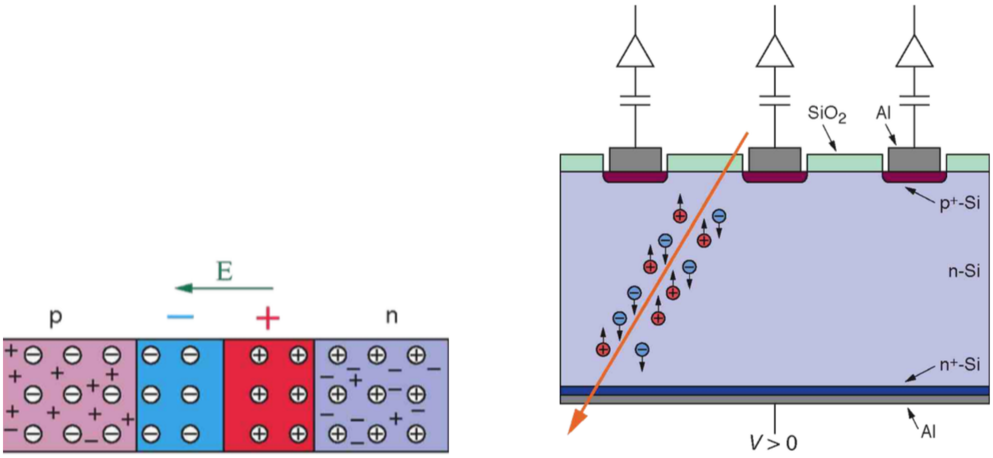

(a) A schematic view of the PN diode. In the middle the depletion layer with mobile charge carriers. [7]

(b) Diode functioning as a sensor. Charged particles create electron-hole pairs, which will drift to electrodes generating a current. [7]

Figure 5

semiconductor with elements containing more electrons, for N-doping, or with less electrons, for P-doping. This process creates free conduction electrons or mobile holes, the lack of an electron which act like a positive electron in the material.

To create a diode a P and N doped semiconductors are pushed together. At the interface an electric field is generated attracting free electrons from the P-type towards the N-type semiconductor, and holes from the N-type towards the P-type semiconductor. This process goes on until both semiconductors are neutral, leaving a depletion layer at the interface with no charge movement. In this region only the ionised free electrons and holes are left after being driven away by the electric field. The diode can be seen in figure 5a.

When charged particles pass through the depletion region $\sim 100/\mu\text{m}$ electron-hole pairs are created [8], as illustrated in figure 5b. These charges are driven towards the electrodes by the electric field, generating a current. When the diode is in reverse bias, the size of the depletion layer can be as large as the sensor thickness allowing large numbers of electron-hole pairs to be produced. The charges are collected on the readout channels, then amplified. The fully depleted operating point for the VeloPix sensor will span between $|V| = 100$ V and 1000 V, with high voltages necessary to compensate the reduction of the depletion layer by the radiation.

The current flowing through the diode in function of the voltage is described by the IV curve, shown in figure 6. Applying a positive voltage will result in a small current, until the internal barrier is reached, then the current grows exponentially. In the reverse bias there is a small leakage current, only due to thermal electron-hole pairs, which quickly reaches a saturation value. If the voltage goes below the breakdown voltage V_{br}, the current increases drastically.

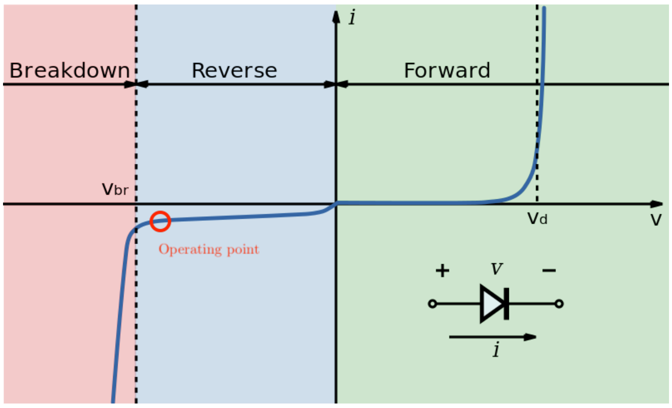

Figure 6: IV curve of a diode. The red circle indicates the operating point for the diode as a sensor. [9]

1.3.2 Effects of irradiation

The saturation current reached in reverse bias increases as the sensor receives more radiation damage. This effect is shown in figure 7. In addition, as the fluence increases, the doping profile changes and modifies the electric field in such a way that a part of the sensor thickness acts as a charge multiplication layer for $|V| > 300$ V, as can be seen in figure 8. This can be seen in figure 9, for large fluence Φ there is an additional contribution with respect to the single PN junction saturation behaviour.

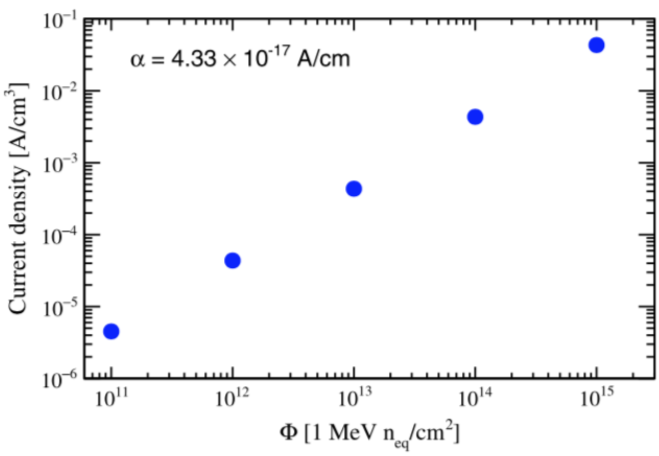

Figure 7: Simulated current per volume at V = -1000 V, as a function of fluence. [10]

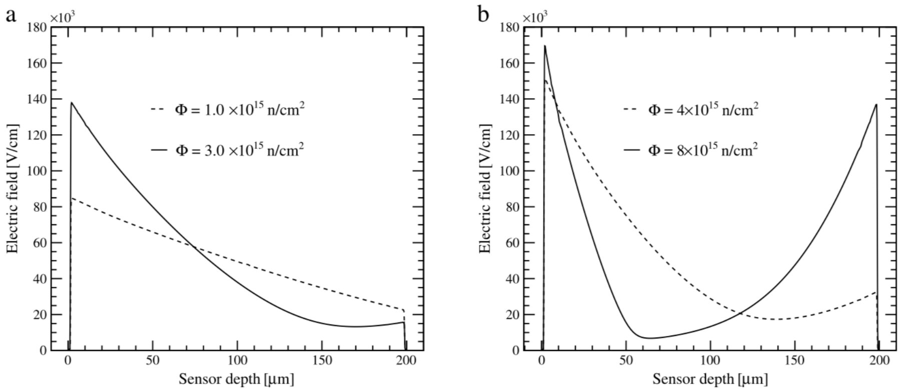

Figure 8: Simulated electric field for different fluent levels for a voltage of $V = 1000$ V. [10]

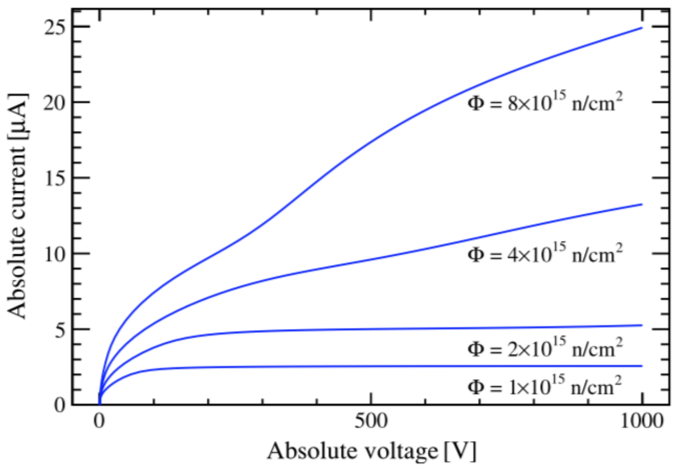

Figure 9: Simulated IV curves for different fluence levels. [10]

2 Motivation

In order to improve or at least maintain the physics performance of the LHCb upgraded detector, the new pixel sensors are placed 5.1 mm away from the proton beam, compared to the 8 mm of the strip sensors. As a consequence, the tip of the sensor will see a very high dose, up to $8 \cdot 10^{15}\ \mathrm{n_{eq}/cm^{-2}}$ fluence , while the external part will only see up to $10^{14}\mathrm{n_{eq}/cm^{-2}}$ along its lifetime. Figure 10 shows the average amount of hits per tile per event with the new setup. The background shows the density of hits.

As a result, the fluence in each pixel will differ, resulting in a different leakage current flowing through the pixels. This effect makes the prediction of the IV curve non trivial [10]. It also imposes working at higher voltages across the diode to keep the sensor fully depleted and leads to more noise in the observations [10]. Measurements of a prototype sensor which has been non uniformly irradiated are shown in figure

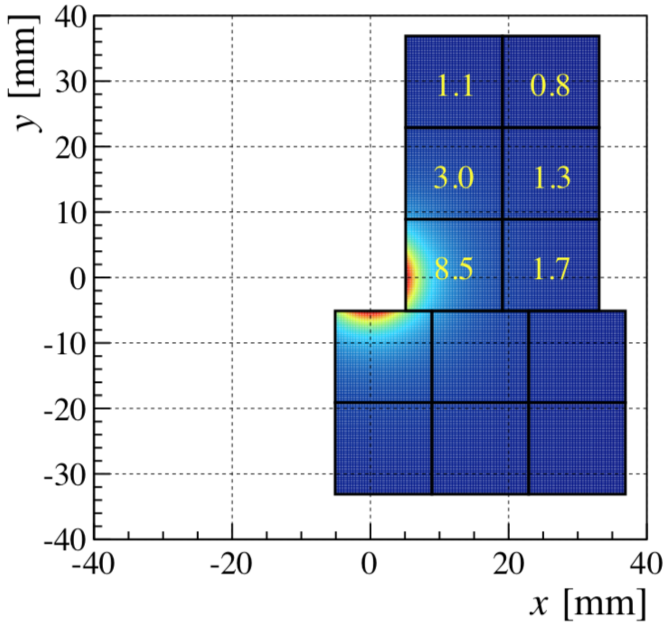

Figure 10: Average amount of hits per ASIC per event. The background shows the density of the hits. [6]

11. The evolution of the current until the breakdown is described accurately by the phenomenological models discussed in section 1.3.2. However the data shows how the breakdown voltage becomes smaller as the temperature rises. Early breakdown occurs at temperature higher than the foreseen operation temperature, this effect needs to be understood.

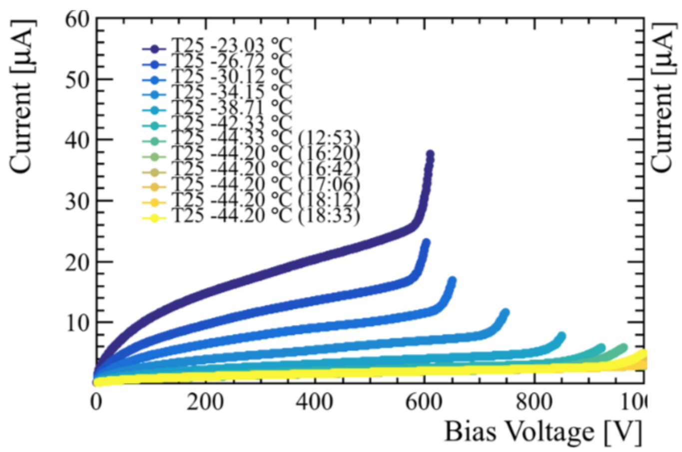

Figure 11: IV curve measurements for a prototype of the VeloPix sensor for non uniform irradiation at different temperatures. [11]

The breakdown seems to be linked to the thermal behaviour of the sensor. A way to test whether this is the case or not is to build a thermal simulation which also takes into account the effect of the non-uniform irradiation in terms of heat generation. The simulation should keep track of various quantities evolving along time such as temperature and current in the sensors and will allow to study the thermal stability of the sensor for a given voltage applied to the diode.

The goal of the simulation is to create a very modular framework which takes into account the thermal conditions of the sensors due the presence of a heat sink and thermal radiation; and allows to simulate the internal heat generation from the radiation damage. The program comes with data generation tools as well as analysis tools, for both an overview of the sensor and local properties.

3 Simulation

The simulation is built upon the method developed by T. Blomberg [12], which uses explicit finite differences. The entire program is made from scratch using PYTHON 2.7 and the libraries NUMPY, MATPLOTLIB. The decision to create the entire framework instead of using some existing tools such as ANSYS, is based on the fact that the simulation is made for a specific case study. The program has been built in a very modular configuration, allowing to add more complexity to the simulation or more realistic geometry than the rectangular box that has been used to develop the program.

The partial differential heat conduction equation in three dimensions is given by,

$$\frac{\partial}{\partial x}\left(\lambda_x \frac{\partial T}{\partial x}\right) + \frac{\partial}{\partial y}\left(\lambda_y \frac{\partial T}{\partial y}\right) + \frac{\partial}{\partial y}\left(\lambda_z \frac{\partial T}{\partial z}\right) + I(x,y,z,t) = C\frac{\partial T}{\partial t}. \tag{1}$$

The thermal conductivities along each direction are given by $\lambda_{x,y,z}$ (W/(m·K)). The term I (W/m^3) represents the internal heat generation and C (J/m^3·K) denotes the volumetric heat capacity. This equation is replaced by a discrete approximation, where temperature is tracked in points in a computational mesh, as shown in figure 12.

The evolution of the tracked quantities are updated after every time step Δt. In each iteration the heat flow, generated heat, current and temperatures are updated. The heat flow $H_{i,j,k}$ (W) in cell (i,j,k) keeps track of the heat extracted from the six adjacent cells and a source term is added for the internal heat generation I. The temperature becomes,

$$T^{new}_{i,j,k} = T^{old}_{i,j,k} + H_{i,j,k}\frac{\Delta t}{\Delta V \cdot C}, \tag{2}$$

where ΔV denotes the volume of the cell. The temperature change in turn affects

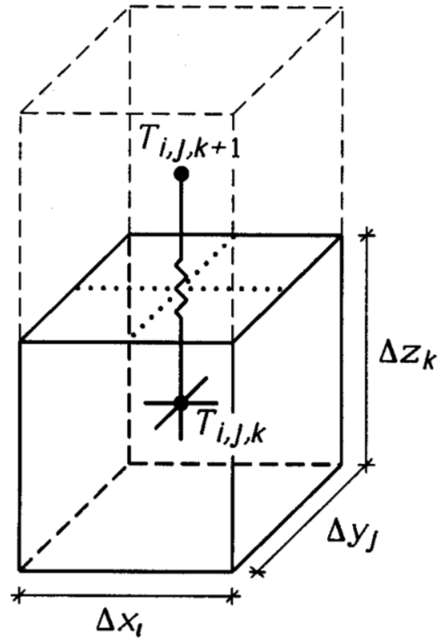

Figure 12: Two cells in the computational mesh. The wiggle indicates a thermal conductance $K_{i,j,k+\frac{1}{2}}$ (W/K). [12]

the current density i (A/m^3) via,

$$i(T^{new}) = i(T^{old}) \left(\frac{T^{new}}{T^{old}}\right)^2 \exp\left\{ -\frac{E_{g,eff}}{2k_B} \left[\frac{1}{T^{new}} - \frac{1}{T^{old}}\right] \right\}. \quad (3)$$

Here k_B is the Boltzmann constant and $E_{g,eff}$ is the effective band gap after irradiation, for silicon the value is $E^{Si}_{g,eff} = 1,2$ eV [10].

In this section the features of the program are discussed in more detail. Section 3.1 describes the physical features implemented and planned improvements. The display capabilities of the program are shown in section 3.2.

3.1 Physics

A simple geometric configuration of the sensor has been used so far, with only three ASICs side by side. The situation of the sensor is shown in figure 13. The sensor is cooled down to $T = 243$ K with a heat sink via convection, represented by a term proportional to $\sim \Delta T$ in the heat flow. The five other sides of the sensor experience heating from radiation at $T = 273$ K where it is assumed the spectrum is from a black body, with a term proportional to $\sim \Delta T^4$.

The current flowing through each cell is modified at initialisation by the fluence. The fluence simulated throughout the sensor is shown in figure 14. The saturation

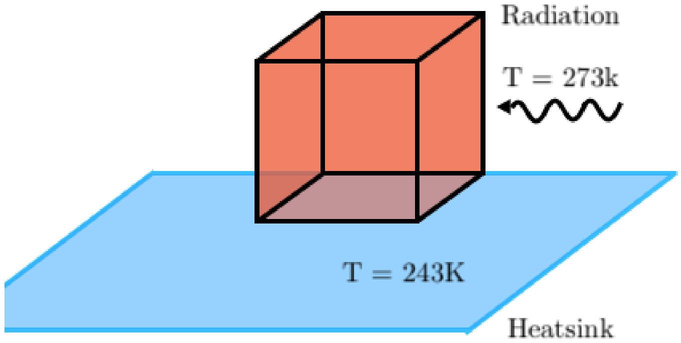

Figure 13: Schematic overview of the sensor. The five sides in red indicate radiation heating at $T = 273$ K, the bottom side is cooled down to $T = 243$ K.

current is then adapted using the damage parameter α,

$$i_s = i_{s,init} + \Phi V \alpha, \tag{4}$$

with Φ (MeV $\mathrm{n_{eq}/m^2}$) the fluence and V the volume of the entire sensor. Note that only the saturation current is increased, the effect from the multiplication of charges is not yet implemented. The Shockley diode equation,

$$i = i_s \left(\mathrm{e}^{\frac{V_{bias}}{n V_T}} - 1 \right), \tag{5}$$

then modifies the current to the applied voltage V_{bias}. Here n is the ideality factor, and the thermal voltage with a value of $V_T = 21.8$ mV at the operating temperature.

This is then used in each iteration to to generate heat internally,

$$P_{internal} = V_{bias} \cdot i. \tag{6}$$

Here an assumption is made that the voltage is distributed equally over all the cells along the z-direction, with each cell experiencing $\Delta V = V_{bias}/N_z$, as in figure 8 for $\Phi = 1 \cdot 10^{15}$ MeV $\mathrm{n_{eq}/m^2}$. In reality the electric field distribution varies with Φ, see figure 8, such that the voltage should be mapped in three dimensions to be complete. This feature will be added later.

3.2 Analysis

The result of the simulation at each time step is stored for later analysis. The framework can display the generated data in two ways, one is more useful to get an overview of the evolution of the system and the other to track the local properties of certain cells.

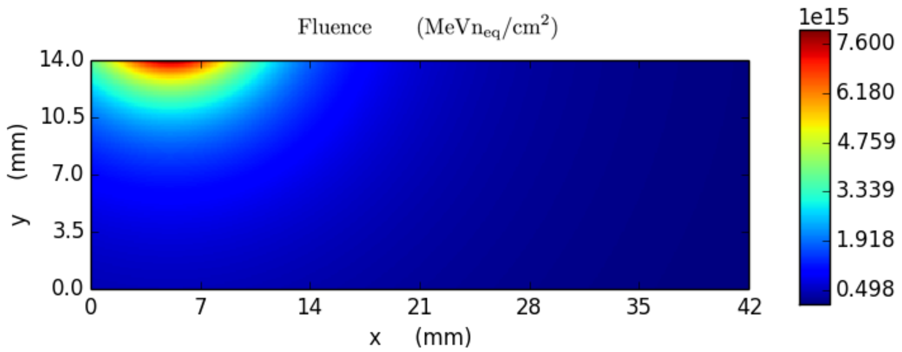

Figure 14: Fluence map of the sensor in the program.

The first method consists in displaying several layers of the sensor in the z-plane as heat maps. In the examples shown here the first layer is the bottom layer with the heat sink below, then the middle layer and finally the top layer. This allows to get an qualitative idea of what is happening inside the sensor without showing an excessive amount of information. The quantities such as temperature, current or heat flow can be visualised this way. For each time step a snapshot is made and put together and saved in a .GIF or .MP4 format. Figure 15 shows four frames from a video format displayed side by side.

The second method to display the data is to track individual cells within a chosen radius. The software then extracts the values of the selected pixels and displays them in a graph such as in figures 16a,16b. This method is more useful to obtain quantitative data.

4 Validation

The framework being built from the ground up needs to be verified to produce physical results. A few case studies have been setup for different features: internal propagation, cooling mechanism (simple), radiation heating and the cooling down of a silicon cube (concrete). The last case study requires a more analytical approach and aims to compare results from certain cells to predictions, while the previous cases only served to verify the mechanism works. In the next sections two of these will be discussed.

4.1 Case study: Internal propagation

For this case study all features except the internal propagation of the temperature have been disabled. A sensor with a total of $N = 1500$ pixels is simulated on a 30x10x5 grid. The core 200 pixels of the sensor are set to $T_1 = 253$ K, while the default temperature is $T_0 = 243$ K for the rest. The initialisation is illustrated in

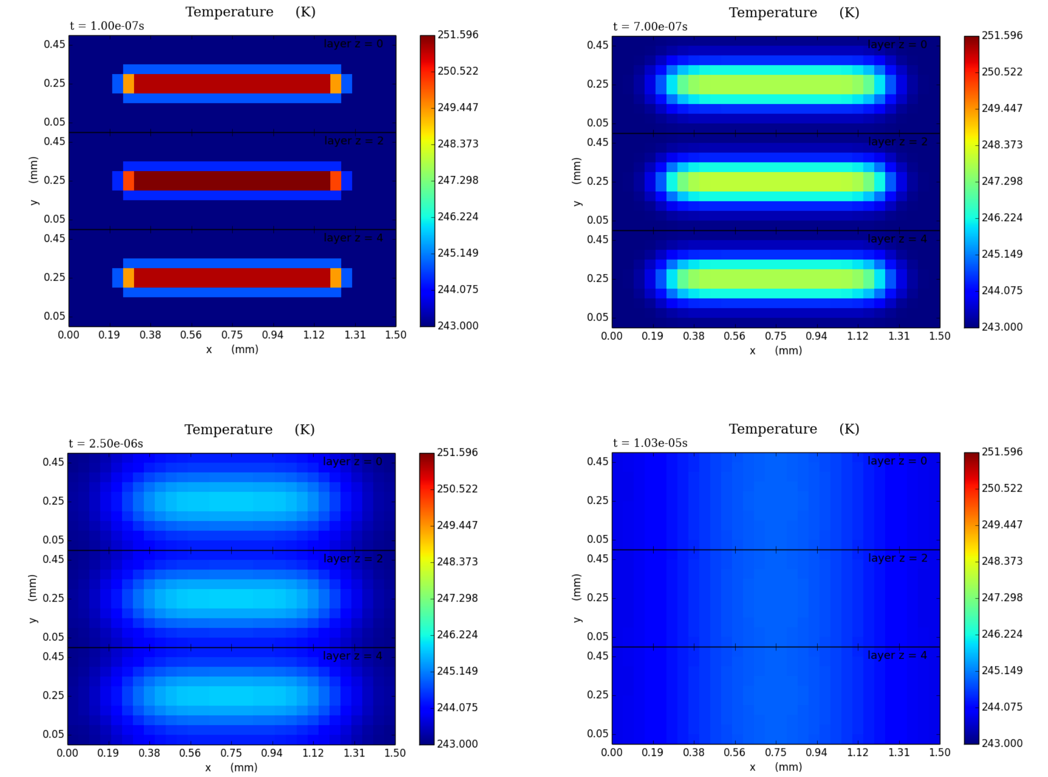

Figure 15: Overview visualisation for four selected frames in a simulation. The heat from the central region can be seen propagating towards the edges and eventually reaching equilibrium.

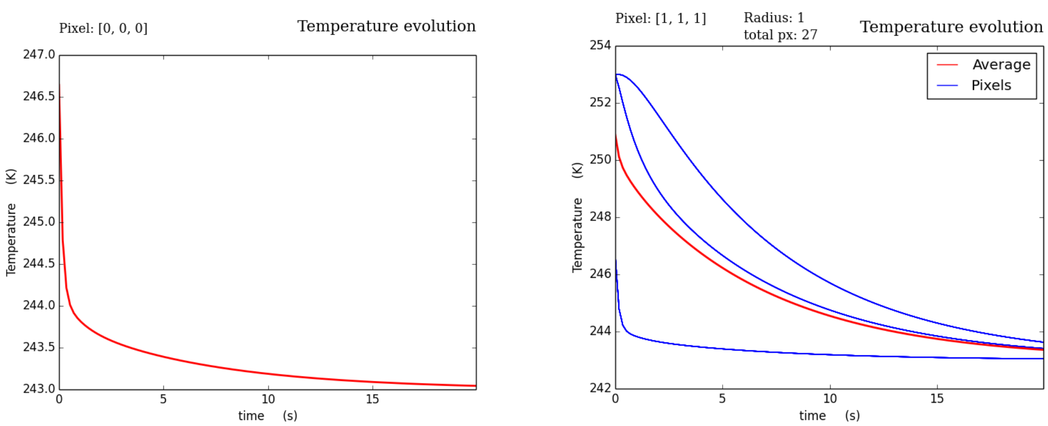

(a) (b)

Figure 16: (a) Temperature evolution for a single cell.
(b) Temperature evolution for a group of pixels, centered around the cell (1,1,1) with a radius of $r = 1$. The blue lines represent all the individual pixels and the red line the average.

figure 17. Four frames of the video format are shown in figure 15. The dissipation of the heat throughout the sensor is clearly visible and behaving as expected.

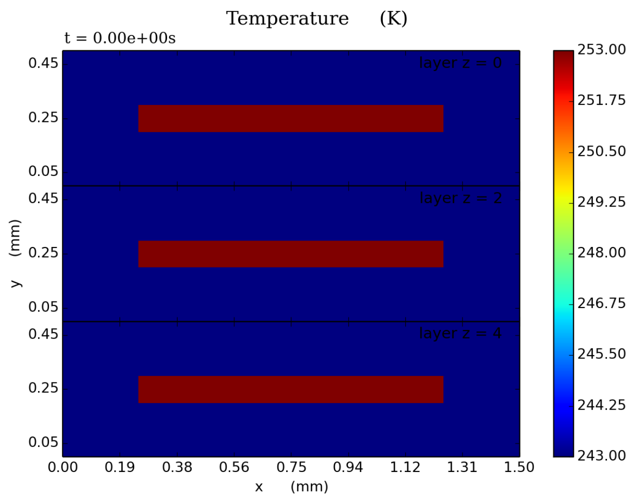

Figure 17: Initialisation of the case study for internal propagation. The central cells are started at 10 degrees higher than the rest of the sensor.

Considering all cells are equivalent, a weighted average of the temperature suffices to produce an expected convergence value:

$$T_{exp} = \frac{N_0 T_0 + N_1 T_1}{N} = \frac{1300 \cdot 243 + 200 \cdot 253}{1500} = 244.33K. \quad (7)$$

This behaviour is observed in figure 18. A small deviation is observed, this is to be expected considering the total amount of cells simulated is small.

4.2 Case study: Cooling mechanism (simple)

For this case study only the internal propagation and the heat sink are activated. The simulation is larger with $N = 37500$ cells on a 150x50x5 grid. The entire sensor is initialised at $T_0 = 253$ K, and the heat sink at T_{sink} =243 K. Two of the pixels are tracked in figure 19. The cell at the bottom immediately cools down and reaches the heat sink value. The cell at the top of the sensor experiences a slight delay as expected. It still reaches the same temperature a short time after.

4.3 Other case studies and finalising the validation

The heating due to thermal radiation has been executed and shows qualitatively that the sensor is heated first from the sides. In order to test the absolute time scales of the simulation, a silicon cube could be cooled down using the heat sink,

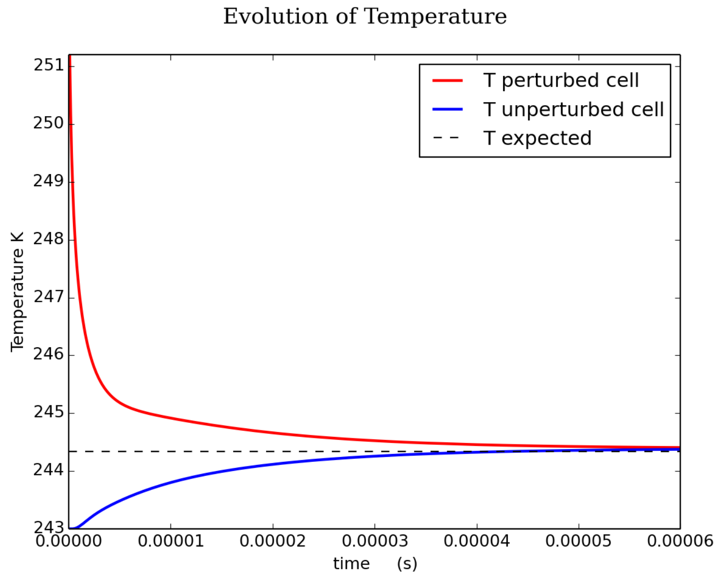

Figure 18: Evolution of the temperature for two pixels, one in the centre (red) and one near the edge (blue). Both converge to the predicted temperature, indicated by the dashed line.

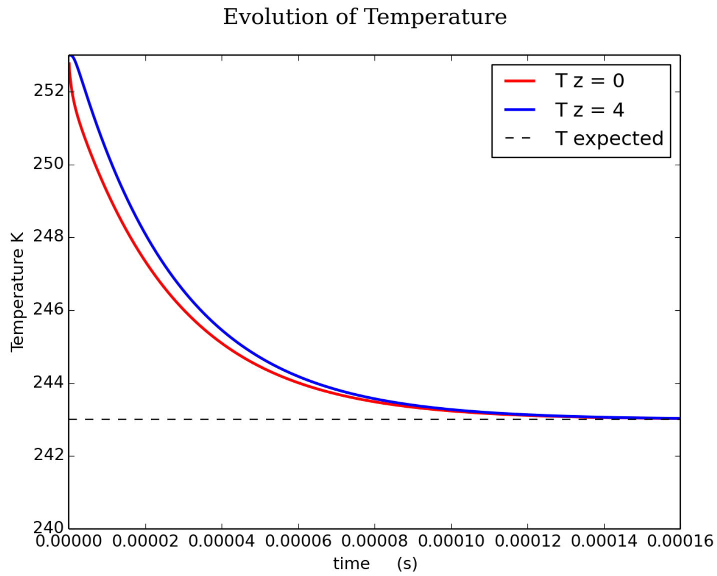

Figure 19: Evolution of the temperature for two pixels, one at the bottom near the heat sink (red) and one at the top (blue). Both reach the temperature of the heat sink indicated by the dashed line. A slight delay can be seen for the blue line as the temperature needs to propagate inside the material before reaching the top layer.

and the temperature evolution compared to simple thermodynamic calculations or another simulation package.

A few more case studies should be performed to finish the validation with a quantitative approach. The internal heat generation due to currents should be verified in more detail. A larger scale thermodynamical example in which the system gets into thermal runaway due to limited cooling should be tested and compared with a thermodynamical prediction.

5 Conclusion

A simulation package was created to test the thermal behaviour of the VeloPix silicon detectors. The software contains tool to generate and store data, as well as analysis tools for a qualitative and quantitative comprehension. The main features of the sensor have already been implemented such as the heat sink, thermal radiation heating and internal heating due to currents. The framework is well documented and was built in a modular way, in order to ease the refinement of features for future developers. The software is public and accessible on gitlab [13]. Several case studies have been executed to test the validity of the code produced.

In the future the program will have to be validated more thoroughly with more concrete situations, as discussed in section 4.3. The software will have to be modified to accommodate for more realistic geometries, allowing different materials next to each other to model the detector assembly. A more refined model to link the radiation effects to the thermal properties will replace the existing simple approximation used in the actual version. For example the change in electric field resulting from the irradiation, as shown in figure 8. In the full framework the program will hopefully help determine the cause of the breakdown in the sensors and identify the operating conditions to respect for the VeloPix.

References

[1] A. A. Alves, Jr. *et al.* [LHCb Collaboration], "The LHCb Detector at the LHC," JINST **3** (2008) S08005. doi:10.1088/1748-0221/3/08/S08005

[2] E. Jans [LHCb Collaboration], "The LHCb detector," arXiv:0910.1740 [hep-ex].

[3] T. Nakada [LHCb Collaboration], "Status of the LHCb Detector Reoptimization," LHCb-2003-006, CERN-LHCb-2003-006, CERN-LHCC-2003-003, LHCC-G-023.

[4] [LHCb Collaboration], "LHCb VELO TDR: Vertex locator. Technical design report," CERN-LHCC-2001-011.

[5] P. C. Tsopelas, "A Silicon Pixel Detector for LHCb,"

[6] LHCb Collaboration, "LHCb VELO Upgrade Technical Design Report," CERN-LHCC-2013-021, LHCB-TDR-013.

[7] M. Krammer, "Silicon detectors," Institute of High Energy Physics, Vienna, Austria, [online], https://www.hephy.at/fileadmin/user_upload/Halbleiterdetektoren.pdf

[8] I. Wingerter, CERN summer student lecture: "Instrumentation and detectors for high energy physics 3, " [Online], https://indico.cern.ch/event/716458/attachments/1680284/2699283/CERNSummerStudents2018-Wingerter-3.pdf

[9] Wikimedia commons user, H1Voltage

[10] Å. Folkestad *et al.*, "Development of a silicon bulk radiation damage model for Sentaurus TCAD," Nucl. Instrum. Meth. A **874** (2017) 94. doi:10.1016/j.nima.2017.08.042

[11] F. Vinicius, "VELO Upgrade IV Update," University of Liverpool

[12] T. Blomberg, "Heat conduction in two and three dimensions," Lund University, Department of Building Physics, (1996)

[13] https://gitlab.cern.ch/cocov/IV_playground